# Conservative discrete-velocity method for the ellipsoidal Fokker-Planck equation in gas-kinetic theory

Sha Liu[1,2,*] Ruifeng Yuan,[2,†] Usman Javid,[2,‡] and Chengwen Zhong[1,2,§]

[1]*National Key Laboratory of Science and Technology on Aerodynamic Design and Research, Northwestern Polytechnical University, Xi'an, Shaanxi 710072, China*

[2]*School of Aeronautics, Northwestern Polytechnical University, Xi'an, Shaanxi 710072, China*

A conservative discrete velocity method (DVM) is developed for the ellipsoidal Fokker-Planck (ES-FP) equation in prediction of nonequilibrium neutral gas flows in this paper. The ES-FP collision operator is solved in discrete velocity space in a concise and quick finite difference framework. The conservation problem of the discrete ES-FP collision operator is solved by multiplying each term in it by extra conservative coefficients whose values are very close to unity. Their differences to unity are in the same order of the numerical error in approximating the ES-FP operator in discrete velocity space. All the macroscopic conservative variables (mass, momentum, and energy) are conserved in the present modified discrete ES-FP collision operator. Since the conservation property in a discrete element of physical space is very important for the numerical scheme when discontinuity and a large gradient exist in the flow field, a finite volume framework is adopted for the transport term of the ES-FP equation. For $nD$-$3V$ ($n < 3$) cases, a $nD$-quasi $nV$ reduction is specifically proposed for the ES-FP equation and the corresponding FP-DVM method, which can greatly reduce the computational cost. The validity and accuracy of both the ES-FP equation and FP-DVM method are examined using a series of $0D$-$3V$ homogenous relaxation cases and $1D$-$3V$ shock structure cases with different Mach numbers, in which $1D$-$3V$ cases are reduced to $1D$-quasi $1V$ cases. Both the predictions of $0D$-$3V$ and $1D$-$3V$ cases match well with the benchmark results such as the analytical Boltzmann solution, direct full-Boltzmann numerical solution, and DSMC result. Especially, the FP-DVM predictions match well with the DSMC results in the Mach 8.0 shock structure case, which is in high nonequilibrium, and is a challenge case of the model Boltzmann equation and the corresponding numerical methods.

## I. INTRODUCTION

The Fokker-Planck (FP) equation with advection-diffusion collision operator is widely used in modeling dynamic systems such as neutral molecule [1–3], plasma [4–6], photonics [7,8], and even biological [9], economic [10], and social [11] systems. The first FP equation for a molecule system is derived from the Boltzmann equation in gas kinetic theory when counting the gazing effect of molecule collisions [12]. The Prandtl (Pr) number yielded from this FP equation is fixed at 3/2. Since the Pr number of real gas is below unity (2/3 for monatomic gas), two types of modified FP equations are proposed. They are the cubic-FP equation [2] and ellipsoidal-FP (ES-FP) equation [3]. Recently, by mapping these FP equations to stochastic differential equations (SDEs), the FP equations are solved in a stochastic and particle way [1,2]. Comparing to other particle methods such as the direct simulation Monte Carlo (DSMC) [13], its computational cost is greatly reduced in the continuum limit (dissipation limit in FP research). Since the mechanism of drag and diffusion

forces holds for both micro and macroscales, then the large time step and cell length can be used. This advantage is very important for the prediction of flow fields in either transitional or continuum regimes where the molecular mean free path (m.f.p.) and mean collision time (m.c.t.) are comparable to or greatly less than the characteristic length and time, respectively. On the other hand, since the deterministic methods are not affected by statistical fluctuation, they are very useful in the precise computation of multiscale nonequilibrium flows, and are helpful in investigating the mechanism of such flows. Moreover, the accuracy of modified FP equations, especially their collision operators, should be examined using a deterministic method.

The first deterministic numerical scheme for FP equation, which can preserve equilibrium, is proposed for a $1V$ (one-dimensional velocity space) isotropic linear Fokker-Planck-Landau (FPL) system [14]. Then it is extended to a mass, energy, and equilibrium preserving scheme [15], $2V$ cases in discrete cylindrical velocity space [16], and nonlinear equation [17,18]. Besides the FPL-type, another form of FP equation is the Rosenbluth-Fokker-Planck equation (RFP) [4]. The RFP equation has a similar mathematical form of the FP equation that is derived from the Boltzmann equation [12]. Its collision operator is written in a differential form with nonlinear advection and diffusion coefficients. By using a finite volume framework in velocity space and extra

*Corresponding author: shaliu@nwpu.edu.cn

†xyrfx@mail.nwpu.edu.cn

‡NormiJavid27@mail.nwpu.edu.cn

§zhongcw@nwpu.edu.cn

coefficients on advection terms for conservation purpose, the RFP equation is well solved by the deterministic numerical method in Refs. [19,20].

Plenty of the FP research focuses on the homogenous FP equation where the particle transport in physical space is assumed to be zero [21]. Several works address the non-homogenous FP equation in the topic of FPL-type equation [22,23]. In flow predictions, the particle transport in physical space is an essential aspect that cannot be ignored. The transport term in the FP equation of gas-kinetic theory (similar to the RFP-type) should be calculated. By taking the particle transport into consideration, the deterministic numerical framework will be the discrete velocity method (DVM). There are several multiscale methods in gas kinetic theory, such as the unified gas-kinetic scheme (UGKS) [24], discrete unified gas-kinetic scheme (DUGKS) [25], gas-kinetic unified algorithm (GKUA) [26], and the improved DVM [27,28], using the DVM framework for predictions of flows from the continuum regime to a rarefied regime. Recently, these methods were widely used in the prediction of nonequilibrium flows [24], plasmas [29], and photonics [30]. Since they used the Bhatnagar-Gross-Krook (BGK)-type model equations, a certain degree of deviation (from the Boltzmann equation) exists in the prediction of high nonequilibrium flows [31], such as the shock structure cases with high Mach (Ma) numbers, which will be calculated in a later section. Since a discrete velocity space is used, the conservation problem of the discrete BGK-type collision operator is addressed by trimming the macroscopic variables that determine the equilibrium state, according to the numerical error of the discrete collision operator [32–35].

In this paper, a novel deterministic method (FP-DVM) is proposed for nonequilibrium flows, which solves the ES-FP equation numerically in the DVM framework. In FP-DVM, the ES-FP collision operator is solved in a deterministic way in discrete velocity space using a framework of the finite difference method (FDM). Instead of considering the conservation in a discrete element of velocity space, the discrete ES-FP collision operator is treated in a relaxation way, and the conservations of mass, momentum, and energy are ensured by coefficients being added to both advection and dissipation terms. The deviations of their values from unity have the same order as the truncation error of the numerical approximation to the ES-FP collision operator. The computational complexity of solving the discrete ES-FP collision operator is $O(N)$, here "$N$" is the number of discrete points in velocity space. Four $0D$-$3V$ ($nD$-$mV$ is a denotation of cases whose dimension of physical space is "$n$" and the dimension of velocity space is "$m$" in the scope of FP research) homogenous relaxation cases and three $1D$-$3V$ shock structure cases with different Ma numbers are conducted to examine the validity and accuracy of both the ES-FP equation and the present numerical method. Using the dimensional reduction method for the ES-FP equation proposed in this paper, $1D$-$3V$ cases are reduced to $1D$-quasi $1V$ cases, and the computational cost is greatly reduced. The remainder of this paper is organized as follows. Section II is a quick review of gas-kinetic theory and FP equation. Section III is the construction of FP-DVM method. Section IV is the numerical experiment. Section V is the discussion and conclusion.

## II. GAS KINETIC THEORY AND FOKKER-PLANCK EQUATION

### A. Distribution function and Boltzmann equation

In gas kinetic theory, the molecular system is described using the distribution function $f(x_i, \xi_j, t)$ depending on location $x_i$, molecular velocity $\xi_j$, and time $t$. It is the number density of molecules that arrived at $x_i$ at time $t$ with velocity $\xi_j$. For dilute gas, the evolution of $f$ is governed by the Boltzmann equation [36]:

$$\frac{\partial f}{\partial t} + \xi_i \frac{\partial f}{\partial x_i} + a_i \frac{\partial f}{\partial \xi_i} = C(f, f), \tag{1}$$

where $a_i$ is the acceleration of a molecule due to a body force such as gravity. The Einstein summation convention is used throughout this paper if without special statement. The left-hand side (LHS) of Eq. (1) is the free transport operator, while the right-hand side (RHS) is the collision operator which is mathematically a five-fold nonlinear integral.

Given the distribution function $f$, macroscopic physical variables, such as mass density $\rho$, momentum density $\rho u_i$ ($u_i$ is macroscopic velocity), energy density $\rho e$ ($e$ is energy per mass), stress $\tau_{ij}$, and heat flux $q_i$, can be obtained using their definition in gas-kinetic theory as follows:

$$\begin{aligned}
\rho &= \langle mf \rangle = mn, \\
\rho u_i &= \langle m\xi_i f \rangle, \\
\rho e &= \langle \tfrac{1}{2} m\xi_k \xi_k f \rangle = \tfrac{1}{2}\rho u_k u_k + \tfrac{3}{2}nkT, \\
\tau_{ij} &= -\langle m(c_i c_j - \tfrac{1}{3} c_k c_k \delta_{ij})f \rangle = -nk(T_{ij} - T\delta_{ij}), \\
q_i &= \langle \tfrac{1}{2} m c_i c_k c_k \rangle,
\end{aligned} \tag{2}$$

where $n$ is number density, $c_i$ is the peculiar velocity defined as $\xi_i - u_i$, $T$ is thermodynamic temperature, $T_{ij}$ is the temperature tensor in gas kinetic theory whose trace is $3T$, $k$ is the Boltzmann constant, $m$ is the mass of a molecule, and $\delta_{ij}$ is the Kronecker delta, the operator $\langle \cdot \rangle$ is an integral over the whole velocity space, which can be written as

$$\langle \cdot \rangle = \int_{-\infty}^{+\infty} \int_{-\infty}^{+\infty} \int_{-\infty}^{+\infty} (\cdot) d\xi_1 d\xi_2 d\xi_3. \tag{3}$$

### B. Fokker-Planck equation for gas kinetic theory

In the scope of gas kinetic theory, the original Fokker-Planck equation without body force is derived in Ref. [12], where the grazing effect of binary collisions is considered. By changing its relaxation rate to $\tau_{\mathrm{FP}} = 2\mu/p$ ($\mu$ is viscosity, $p$ is pressure), the standard Fokker-Planck equation as a model of the Boltzmann equation can be written as follows:

$$\frac{\partial f}{\partial t} + \xi_i \frac{\partial f}{\partial x_i} = \frac{1}{\tau_{\mathrm{FP}}} \left\{ \frac{\partial((\xi_i - u_i)f)}{\partial \xi_i} + RT\delta_{ij} \frac{\partial^2 f}{\partial \xi_i \partial \xi_j} \right\}, \tag{4}$$

where $R = k/m$ is the specific gas constant. Since the standard Fokker-Planck equation corresponds to a fix Prandtl number of 3/2, two types of modified Fokker-Planck equations, the cubic-FP equation equation [2] and ES-FP equation [3], are proposed. In cubic-FP, the advection term is multiplied by a polynomial of molecular velocity $\xi_i$, whose coefficients are used to get the right relaxation rate of both stress and

heat flux, thus a right Prandtl is realized. In ES-FP equation, the diagonal dissipation coefficient $RT\delta_{ij}$ in the standard FP equation is replaced by $T_{\text{ES},ij}$ which is defined as follows:

$$T_{\text{ES},ij} = (1-\nu)T\delta_{ij} + \nu T_{ij}, \qquad (5)$$

as a combination of isotropic temperature $T$ and anisotropic temperature $T_{ij}$ ($T_{ij} = \langle mc_ic_jf\rangle/\rho R$), and $\nu$ is defined as

$$\nu = \max\left(-\frac{5}{4}, -\frac{T}{\lambda_{\max}-T}\right), \qquad (6)$$

where $\lambda_{\max}$ is the maximum eigenvalue of the positive definite matrix $T_{ij}$. Since $\nu$ and the Pr number have the following relation:

$$\text{Pr} = \frac{3}{2(1-\nu)}, \qquad (7)$$

the Pr number is 2/3 except in the extreme condition $\lambda_{\max} > 1.8T$. In this extreme condition, Pr varies from 2/3 to unity. The relaxation time $\tau_{\text{ES}}$ in the ES-FP collision operator is defined as

$$\tau_{\text{ES}} = 2(1-\nu)\frac{\mu}{p}. \qquad (8)$$

Since the procedure of deriving ES-FP equation from the standard FP equation is similar to that of extending the BGK equation to the ES-BGK equation, it is called the ES-FP in Ref. [3]. Similar to the standard FP, ES-FP is written in the following form:

$$\frac{\partial f}{\partial t} + \xi_i\frac{\partial f}{\partial x_i} = \frac{1}{\tau_{\text{ES}}}\left\{\frac{\partial((\xi_i-u_i)f)}{\partial \xi_i} + RT_{\text{ES},ij}\frac{\partial^2 f}{\partial \xi_i\partial \xi_j}\right\}. \qquad (9)$$

## III. DETERMINISTIC DISCRETE VELOCITY METHOD FOR ELLIPSOIDAL FOKKER-PLANCK EQUATION

In the DVM framework, the physical space $x_i$, the velocity space $\xi_i$, and the time $t$ are discrete. The ES-FP equation is solved in an operator splitting way. The free transport operator [LHS of Eq. (9)] is solved in the physical space first to get the distribution $f^*$ at intermediate step in each discrete element in physical space. Given $f^*$, the collision operator [RHS of Eq. (9)] can be solved in the discrete velocity space, then the distribution can be evolved to the next time step.

### A. Free transport operator

For a numerical scheme in flow predictions, the conservation property in a discrete cell (in physical space) is very important when discontinuity, such as the shock wave, exists in the flow field. So the transport operator of the ES-FP equation is solved in a finite volume framework where the extra numerical viscosity needed by capturing the discontinuity is provided by the slope limiters. In this paper, a Euler method is used for temporal discretization. Second-order upwind reconstruction in physical space is used for the flux term. The FVM-type numerical scheme for the transport operator can be written as

$$\frac{f^*-f^n}{\Delta t} + \frac{1}{\Omega}\sum_{a=1}^{A}(\xi_if_a)S_{a,i} = 0, \qquad (10)$$

where

$$f_a = f^n + \frac{\partial f^n}{\partial x_j}(x_{a,j}-x_{c,j}). \qquad (11)$$

In Eq. (10), $S_{a,i}$ is the cell interface whose direction is from the inside to outside. Its subscript "$a$" is an index of the discrete cell interface, and the total number of discrete interfaces in a cell is denoted by "$A$". $\Omega$ is the volume of the cell. $\Delta t$ is the time interval. The superscript "$n$" denotes the $n$th iteration step, and "$*$" denotes the intermediate time step between the $n$th and $(n+1)$th steps in the operator splitting treatment. In Eq. 11, the subscript "$c$" denotes the "cell center". In the present method, the calculation of slope $\partial f/\partial x_j$ is to the second order, and the van Leer slope limiter is used.

### B. Collision operator

The collision operator is solved in a finite difference framework since it is computationally efficient. It should be noted that the free transport operator is treated in a finite volume framework to make the transport process conservative when discontinuity occurs in the flow field. Theoretically, the evolution equation of collision operator can be directly written using the information at intermediate time step as follows:

$$\frac{f^{n+1}-f^*}{\Delta t} = \frac{1}{\tau_{\text{ES}}^*}\left\{\frac{\partial((\xi_i-u_i^*)f^*)}{\partial \xi_i} + RT_{\text{ES},ij}^*\frac{\partial^2 f^*}{\partial \xi_i\partial \xi_j}\right\}, \qquad (12)$$

where the first- and second-order slopes in velocity space can be numerically approximated using the central difference.

The numerical approximation to the slopes has a truncation error related to $\Delta\xi$. If a second-order central difference is used, the truncation error is $O(\Delta\xi^2)$. The numerical quadratures in velocity space also generate numerical errors. If the above numerical scheme for the ES-FP collision operator is directly used without treatment of these numerical errors, the aggregate effect will produce undesired variations of mass, momentum, and energy which should be zero since the collision operator fulfills the conservation property. As a result, it often leads to a nonconvergent and nonconservative numerical scheme. This problem is addressed in several works on the topic of the FPL equation [6,37]. For the RFP equation which has a similar mathematical form as the FP and ES-FP equations used in gas-kinetic theory, the authors of Ref. [19] constructed a conservative finite volume scheme in velocity space.

In this paper, the nonconvergence problem for the efficient finite difference framework is handled in a similar way as Ref. [19] as follows. Because in a finite difference framework in velocity space, the distribution function only lives at discrete nodes, the corresponding discrete collision operator should be slightly different from the continuous one due to the inevitable numerical errors. First, the collision operator is rewritten as follows by decomposing the advection term into a distribution function and a first-order slope

$$\frac{\partial f}{\partial t} = \frac{1}{\tau_{\text{ES}}}\left\{3f + (\xi_i-u_i)\frac{\partial f}{\partial \xi_i} + RT_{\text{ES},ij}\frac{\partial^2 f}{\partial \xi_i\partial \xi_j}\right\}. \qquad (13)$$

Then each term in the brace is multiplied by a coefficient $\varepsilon$ which is designed to eliminate the influence of numerical errors on conservation property, and the collision operator turns into

$$\frac{\partial f}{\partial t} = \frac{1}{\tau_{ES}}\left\{3\varepsilon_F f + \varepsilon_{A,i}(\xi_i - u_i)\frac{\partial f}{\partial \xi_i} + \varepsilon_D R T_{ES,ij}\frac{\partial^2 f}{\partial \xi_i \partial \xi_j}\right\}. \tag{14}$$

The values of $\varepsilon_F$, $\varepsilon_{A,i}$, and $\varepsilon_D$ are very close to unity, and their departures from unity (denoted by $|\varepsilon - 1|$) are directly related to the numerical error. Being similar to Ref. [19], the treatment

of $\varepsilon_{A,i}$ is as follows:

$$\begin{aligned}\varepsilon_{A,i} &\neq 1, \xi_i < 0,\\ \varepsilon_{A,i} &= 1, \xi_i \geqslant 0.\end{aligned} \tag{15}$$

That means that $\varepsilon_{A,i}$ only exerts on half of the velocity space. For continuous velocity space, these $\varepsilon$ become unity since it is the basic property of ES-FP equation that mass, momentum, and energy conservations are fulfilled. For discrete velocity space, these coefficients can be obtained using the conservation of mass, momentum, and energy, and solving the following algebraic equations analytically:

$$\varepsilon_F \sum 3f + \varepsilon_{A,1}\sum_{\xi_1<0} A_1 + \varepsilon_{A,2}\sum_{\xi_2<0} A_2 + \varepsilon_{A,3}\sum_{\xi_3<0} A_3 + \varepsilon_D \sum D = -\left(\sum_{\xi_1\geqslant 0} A_1 + \sum_{\xi_2\geqslant 0} A_2 + \sum_{\xi_3\geqslant 0} A_3\right),$$

$$\varepsilon_F \sum 3\xi_1 f + \varepsilon_{A,1}\sum_{\xi_1<0} \xi_1 A_1 + \varepsilon_{A,2}\sum_{\xi_2<0} \xi_1 A_2 + \varepsilon_{A,3}\sum_{\xi_3<0} \xi_1 A_3 + \varepsilon_D \sum \xi_1 D = -\left(\sum_{\xi_1\geqslant 0} \xi_1 A_1 + \sum_{\xi_2\geqslant 0} \xi_1 A_2 + \sum_{\xi_3\geqslant 0} \xi_1 A_3\right),$$

$$\varepsilon_F \sum 3\xi_2 f + \varepsilon_{A,1}\sum_{\xi_1<0} \xi_2 A_1 + \varepsilon_{A,2}\sum_{\xi_2<0} \xi_2 A_2 + \varepsilon_{A,3}\sum_{\xi_3<0} \xi_2 A_3 + \varepsilon_D \sum \xi_2 D = -\left(\sum_{\xi_1\geqslant 0} \xi_2 A_1 + \sum_{\xi_2\geqslant 0} \xi_2 A_2 + \sum_{\xi_3\geqslant 0} \xi_2 A_3\right), \tag{16}$$

$$\varepsilon_F \sum 3\xi_3 f + \varepsilon_{A,1}\sum_{\xi_1<0} \xi_3 A_1 + \varepsilon_{A,2}\sum_{\xi_2<0} \xi_3 A_2 + \varepsilon_{A,3}\sum_{\xi_3<0} \xi_3 A_3 + \varepsilon_D \sum \xi_3 D = -\left(\sum_{\xi_1\geqslant 0} \xi_3 A_1 + \sum_{\xi_2\geqslant 0} \xi_3 A_2 + \sum_{\xi_3\geqslant 0} \xi_3 A_3\right),$$

$$\varepsilon_F \sum 3\xi^2 f + \varepsilon_{A,1}\sum_{\xi_1<0} \xi^2 A_1 + \varepsilon_{A,2}\sum_{\xi_2<0} \xi^2 A_2 + \varepsilon_{A,3}\sum_{\xi_3<0} \xi^2 A_3 + \varepsilon_D \sum \xi^2 D = -\left(\sum_{\xi_1\geqslant 0} \xi^2 A_1 + \sum_{\xi_2\geqslant 0} \xi^2 A_2 + \sum_{\xi_3\geqslant 0} \xi^2 A_3\right),$$

where $A_i$ $(i = 1, 2, 3)$ and $D$ are defined as

$$A_i = (\xi_i - u_i)\frac{\partial f}{\partial \xi_i}, \quad D = R T_{ES,ij}\frac{\partial^2 f}{\partial \xi_i \partial \xi_j}. \tag{17}$$

In Eq. (16), the numerical integrals in whole velocity space and half velocity space are denoted by $\sum(\cdot)$, $\sum_{\xi_i<0}(\cdot)$, and $\sum_{\xi_i\geqslant 0}(\cdot)$, respectively. Take index $i = 1$, for example, these integrals are in the following form:

$$\sum(\cdot) = \sum_{\xi_1\in(\xi_{1,\min},\xi_{1,\max})}\sum_{\xi_2\in(\xi_{2,\min},\xi_{2,\max})}\sum_{\xi_3\in(\xi_{3,\min},\xi_{3,\max})}(\cdot)\Delta\xi_1\Delta\xi_2\Delta\xi_3,$$

$$\sum_{\xi_1<0}(\cdot) = \sum_{\xi_1\in(\xi_{1,\min},0)}\sum_{\xi_2\in(\xi_{2,\min},\xi_{2,\max})}\sum_{\xi_3\in(\xi_{3,\min},\xi_{3,\max})}(\cdot)\Delta\xi_1\Delta\xi_2\Delta\xi_3,$$

$$\sum_{\xi_1\geqslant 0}(\cdot) = \sum_{\xi_1\in[0,\xi_{1,\max})}\sum_{\xi_2\in(\xi_{2,\min},\xi_{2,\max})}\sum_{\xi_3\in(\xi_{3,\min},\xi_{3,\max})}(\cdot)\Delta\xi_1\Delta\xi_2\Delta\xi_3. \tag{18}$$

where the subscript "min" and "max" denote the boundaries in each direction of truncated velocity space.

Finally, the evolution of the distribution function according to the discrete ES-FP collision operator can be written as

$$\frac{f^{n+1} - f^*}{\Delta t} = \frac{1}{\tau_{ES}^*}\left\{3\varepsilon_F^* f^* + \varepsilon_{A,i}^*(\xi_i - u_i^*)\frac{\partial f^*}{\partial \xi_i} + \varepsilon_F^* R T_{ES,ij}^*\frac{\partial^2 f^*}{\partial \xi_i \partial \xi_j}\right\}. \tag{19}$$

The calculation process of the collision operator can be summed up as follows. First, using the information $f^*$ at the intermediate step, the first- and second-order slopes (in velocity space) in Eq. (19) can be calculated and stored. Then the contribution of each term in the brace of Eq. (19) to mass, momentum, and energy can be calculated using numerical

integration in Eq. (18). In the process of numerical integration, $u_i$ and $T_{ij}$ can also be obtained as

$$T_{ij}^* = \frac{\sum c_i c_j f^*}{R\sum f^*}, \quad u_i^* = \frac{\sum \xi_i f^*}{\sum f^*}. \tag{20}$$

Then, using the obtained numerical integrals, the coefficient $\varepsilon^*$ can be calculated using Eq. (16). Up to this point, every term in Eq. (19) is obtained, and the distribution function can be updated to the $(n + 1)$th time step.

### C. Reduced ES-FP equation

Real monatomic gas flows have a three-dimensional physical space and a three-dimensional velocity space (3D-3V case). For the $nD$-3V case where $n < 3$, the ES-FP equation can be reduced to the $nD$-quasi $nV$ case whose computational cost is greatly reduced. The reduction method used in ES-FP is the same with that used for reducing the BGK-type model equations in several numerical schemes [38–41], which splits the distribution function into a mass distribution and an energy distribution, and splits the BGK-type equation into two equations for mass distribution and energy distribution, respectively. The following context takes the reducing process from the 1D-3V case to the 1D-quasi 1V case, for example (which is also used in the case of shock wave structure calculation in this paper). For the 1D case in the $x_1$ direction, there is

$$\frac{\partial f}{\partial x_2} = 0, \quad \frac{\partial f}{\partial x_3} = 0,$$
$$u_2 = 0, \quad u_3 = 0,$$

$$T_{12} = T_{21} = 0, \quad T_{23} = T_{32} = 0, \quad T_{13} = T_{31} = 0,$$
$$T_{22} = T_{33} = (3T - T_{11})/2. \tag{21}$$

The slopes in $x_2$ and $x_3$ directions are zero. The off-diagonal elements in temperature tensor $T_{ij}$ are zero because the tangential stress is zero [according to Eq. (2)].

The ES-FP equation can be first reduced to

$$\frac{\partial f}{\partial t} + \xi_1 \frac{\partial f}{\partial x_1} = \frac{1}{\tau_{ES}} \left\{ 3f + (\xi_1 - u_1)\frac{\partial f}{\partial \xi_1} + \xi_2 \frac{\partial f}{\partial \xi_2} + \xi_3 \frac{\partial f}{\partial \xi_3} \right. $$
$$\left. + RT_{ES,11}\frac{\partial^2 f}{\partial \xi_1^2} + RT_{ES,22}\frac{\partial^2 f}{\partial \xi_2^2} + RT_{ES,33}\frac{\partial^2 f}{\partial \xi_3^2} \right\}. \tag{22}$$

Define a mass distribution and an energy distribution in the $\xi_1$ axis as follows:

$$F = \int_{-\infty}^{+\infty} \int_{-\infty}^{+\infty} mf d\xi_2 d\xi_3,$$
$$G = \int_{-\infty}^{+\infty} \int_{-\infty}^{+\infty} m(\xi_2^2 + \xi_3^2)f d\xi_2 d\xi_3. \tag{23}$$

Then multiply the ES-FP equation by unity and $\xi_2^2 + \xi_3^2$, and integrate it in both $\xi_2$ and $\xi_3$ directions. After calculating the integrals, the reduced ES-FP equation becomes a system of two equations about "$F$" and "$G$" as follows:

$$\frac{\partial F}{\partial t} + \xi_1 \frac{\partial F}{\partial x_1} = \frac{1}{\tau_{ES}} \left\{ F + (\xi_1 - u_1)\frac{\partial F}{\partial \xi_1} + RT_{ES,11}\frac{\partial^2 F}{\partial \xi_1^2} \right\},$$
$$\frac{\partial G}{\partial t} + \xi_1 \frac{\partial G}{\partial x_1} = \frac{1}{\tau_{ES}} \left\{ G + (\xi_1 - u_1)\frac{\partial G}{\partial \xi_1} - 2G + RT_{ES,11}\frac{\partial^2 G}{\partial \xi_1^2} + 2R(T_{ES,22} + T_{ES,33})F \right\}. \tag{24}$$

Then the solving of $f$ in three-dimensional velocity space is turned into the solving of $F$ and $G$ in one-dimensional velocity space. Here the evolutions of $F$ and $G$ are coupled through a relaxation process from $2G$ to $2R(T_{ES,22} + T_{ES,33})F$ in the second equation ($G$ equation) in Eq. (24). If the integrated equation is Eq. (14) (the discrete form), $\varepsilon$ will appear in the corresponding terms in both the $F$ and $G$ equations in Eq. (24). Practically, these $\varepsilon$ can only appear in the $F$ equation since it can be seen from the later equation [Eq. (27)] that both mass and momentum conservations are only involved by $F$, and $F$ also appears in the expression of energy conservation. So the reduced ES-FP equations in discrete velocity space can be written as

$$\frac{\partial F}{\partial t} + \xi_1 \frac{\partial F}{\partial x_1} = \frac{1}{\tau_{ES}} \left\{ \varepsilon_F F + \varepsilon_{A,1}(\xi_1 - u_1)\frac{\partial F}{\partial \xi_1} + \varepsilon_D RT_{ES,11}\frac{\partial^2 F}{\partial \xi_1^2} \right\},$$
$$\frac{\partial G}{\partial t} + \xi_1 \frac{\partial G}{\partial x_1} = \frac{1}{\tau_{ES}} \left\{ G + (\xi_1 - u_1)\frac{\partial G}{\partial \xi_1} - 2G + RT_{ES,11}\frac{\partial^2 G}{\partial \xi_1^2} + 2R(T_{ES,22} + T_{ES,33})F \right\}, \tag{25}$$

here, in the 1D case, the "A" and "D" in Eq. (17) are reduced to

$$A_1 = (\xi_1 - u_1)\frac{\partial F}{\partial \xi_1},$$
$$D = RT_{ES,11}\frac{\partial^2 F}{\partial \xi_1 \partial \xi_1}. \tag{26}$$

Using conservations of mass, momentum, and energy, the $\varepsilon$ for conservation purpose can be obtained by solving the following linear equations:

$$\varepsilon_F \sum F + \varepsilon_{A,1} \sum_{\xi_1<0} A_1 + +\varepsilon_D RT_{\text{ES},11} \sum D_{11} = -\left( \sum_{\xi_1<0} A_1 \right),$$

$$\varepsilon_F \sum \xi_1 F + \varepsilon_{A,1} \sum_{\xi_1<0} \xi_1 A_1 + \varepsilon_D RT_{\text{ES},11} \sum \xi_1 D_{11} = -\left( \sum_{\xi_1<0} \xi_1 A_1 \right), \quad (27)$$

$$\varepsilon_F \sum \xi_1^2 F + \varepsilon_{A,1} \sum_{\xi_1<0} \xi_1^2 A_1 + \varepsilon_D RT_{\text{ES},11} \sum \xi_1^2 D_{11} = -\left( \sum_{\xi_1<0} \xi_1^2 A_1 + \sum \text{RHS}_G \right),$$

here $\text{RHS}_G$ is the RHS of the $G$ equation [Eq. (25)]. The numerical process for the $1V$ case is the same with the $3V$ case in Secs. III A and III B, expect that the operation of $f$ is now on $F$ and $G$.

### D. Numerical error in discrete Fokker-Planck collision operator

The numerical error in discrete velocity space comes from the three items below:

(1) The truncation in velocity space;

(2) The error in numerical integration; and

(3) The truncation error in calculating the slopes using discrete points.

For the first item, the domain of truncated velocity space should be as large as possible. But to achieve high computational efficiency, it cannot be too large. The Maxwellian distribution suggests that the domain should be at least larger than $3\sqrt{RT}$ since beyond $3\sqrt{RT}$ the distribution only contributes 0.3% of mass.

For the second item, high-order numerical integration can be used, such as the Newton-Cotes integration, to suppress the

numerical error in this item. While for the sake of clarity, the rectangular integration is used in this paper.

For the third item, a high-order central difference can be used, which will be analyzed in Sec. IV A. Much of its influence is on the order of the departure of $\varepsilon$ from unity. A too high-order central difference will harm the computational efficiency.

## IV. NUMERICAL EXPERIMENT

### A. Maintain the thermal equilibrium Maxwellian distribution (0D-3V case)

In this case, the initial distribution function is the Maxwellian distribution $g$ in the following form:

$$g = n\left(\frac{m}{2\pi kT}\right)^{3/2} \exp\left(-\frac{mc_i c_i}{2kT}\right). \quad (28)$$

If a discrete numerical method is conservative, the distribution function will maintain the Maxwellian distribution.

Using this case, the numerical stability of the present method is examined. The validity of conservative coefficients $\varepsilon$ and the accuracy of the present scheme are also investigated. For Maxwellian distribution, $n = 1$, $u_i = 0$, and $T = 1$ are chosen. The domain of truncated velocity space in each direction is $[-5, 5]$. Both $50 \times 50 \times 50$ and $100 \times 100 \times 100$ meshes in velocity space are tested. Both second- and fourth-order central difference are used in approximating the first- and second-order slopes in the ES-FP collision operator. The maintained distribution functions that are predicted using
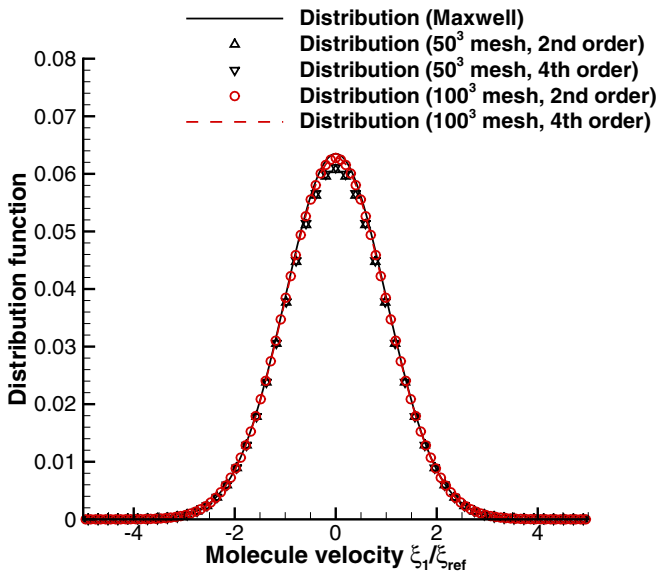


FIG. 1. Stable Maxwellian distribution computed by FP-DVM on $50^3$ and $100^3$ uniform meshes.

TABLE I. Macroscopic variables and $\varepsilon$ at different settings.

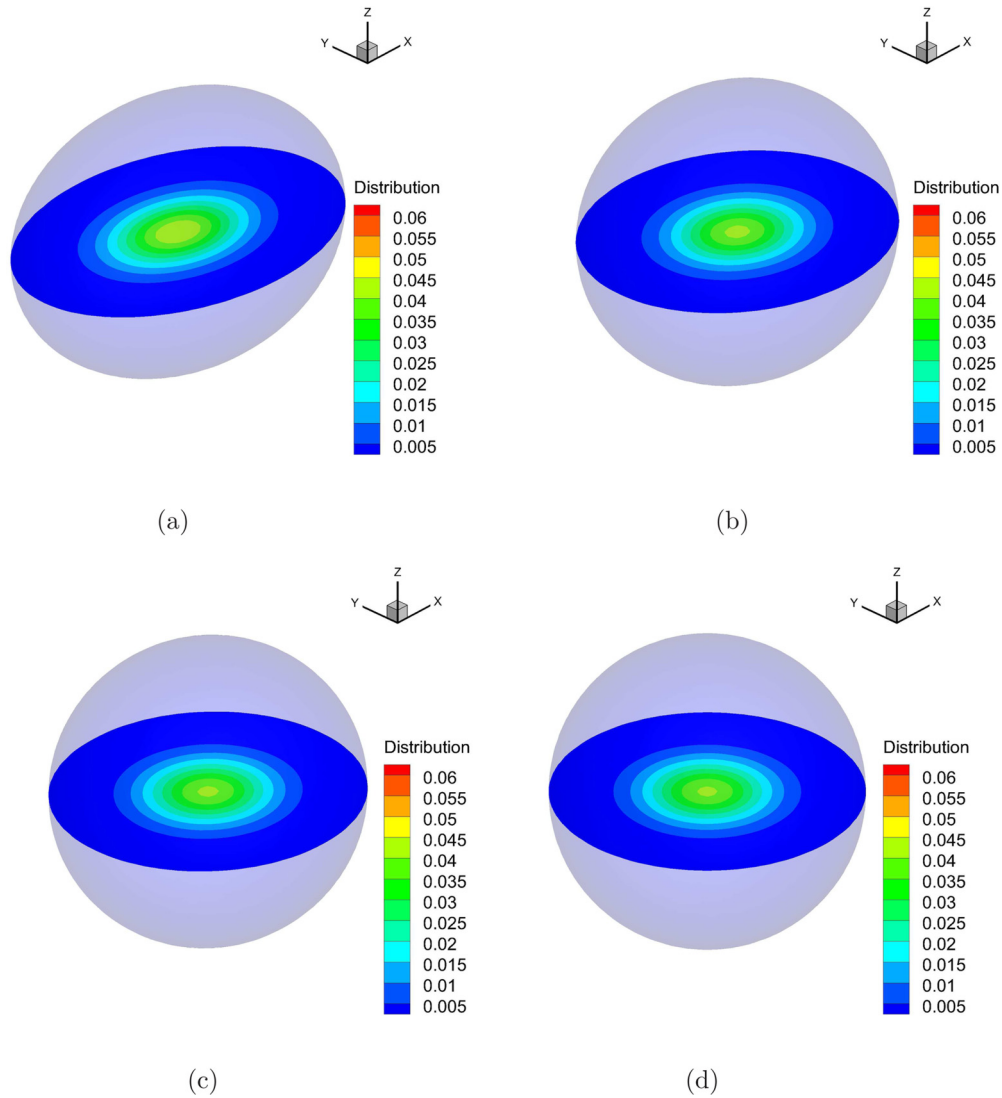| | $50^3$ mesh 2nd order | $50^3$ mesh 4th order | $100^3$ mesh 2nd order | $100^3$ mesh 4th order |
|---|---|---|---|---|
| $|\rho - 1|$ | $8.5e-5$ | $8.5e-5$ | $1.3e-5$ | $1.2e-5$ |
| $|u_1|$ | $5.0e-5$ | $5.0e-5$ | $4.7e-6$ | $2.0e-17$ |
| $|T - 1|$ | $5.2e-4$ | $5.2e-4$ | $9.5e-5$ | $9.1e-5$ |
| $|\varepsilon_f - 1|$ | $7.7e-5$ | $4.6e-5$ | $4.5e-6$ | $2.1e-7$ |
| $|\varepsilon_{A,1} - 1|$ | $3.0e-5$ | $7.4e-5$ | $1.1e-6$ | $8.9e-16$ |
| $|\varepsilon_D - 1|$ | $2.0e-2$ | $6.4e-4$ | $5.0e-3$ | $9.3e-5$ |
| $\log|\varepsilon_f - 1|/\log \Delta\xi$ | $5.8$ | $6.2$ | $5.3$ | $6.7$ |
| $\log|\varepsilon_{A,1} - 1|/\log \Delta\xi$ | $6.5$ | $5.9$ | $6.0$ | $15.0$ |
| $\log|\varepsilon_D - 1|/\log \Delta\xi$ | $2.4$ | $4.6$ | $2.3$ | $4.0$ |

FIG. 2. The relaxation process of distribution with initial anisotropic temperatures, only the region with distribution function greater than $5 \times 10^{-3}$ is plotted, and the contour is on the plane $\xi_3 = 0$. The evolution time $\tau$ is (a) 0, (b) 1, (c) 2, and (d) 10, respectively, in clockwise from the top-left figure.

$50 \times 50 \times 50$ and $100 \times 100 \times 100$ meshes are shown in the radial direction in Fig. 1, respectively. Although the distribution on $50 \times 50 \times 50$ meshes slightly deviates from the analytical Maxwellian distribution near the zero point, it is stable since the discrete ES-FP is conservative. In Table I, there is a comparison of integral error and $\varepsilon$ under dense or coarse meshes and using low- or high-order central difference for calculating slopes. It can be seen that integral error ($|\rho - 1|$, $|u_1|$, $|T - 1|$) is related to the mesh number, and almost has no relation to the order of central difference. Comparing to the coarse mesh, by using a dense mesh, the precision of macroscopic variables will increase, while the computational cost will also increase. To increase the integration precision, the high-order integration method such as Newton-Cotes can be used without using a dense mesh. While for clarity, the direct rectangular integration is used in this paper. Using either a dense mesh or a higher-order difference will make the deviation of $\varepsilon$ from unity a smaller value. The largest deviation comes from $\varepsilon_D$. From the *log* data, it can be seen that

when fourth-order difference is used, the order of $|\varepsilon_D - 1|$ is about 4, while for a second-order difference, it is about 2. This data show that the order of $|\varepsilon_D - 1|$ is related to the order of numerical difference, and is almost not affected by the mesh number. In the following test cases, the second-order central difference is used in the velocity space for efficiency.

### B. Energy relaxation among directions (0*D*-3*V* case)

In this case, initially the temperatures in different directions are not the same (anisotropic temperature). Through molecular collisions, these temperatures will gradually achieve equilibrium during several m.c.t. Here the initial temperatures are set to be $T_1 = 2.0$, $T_2 = 1.0$, $T_3 = 1.0$. The truncated discrete velocity space is $[-7, 7]$ in each direction with 70 discrete points ($70 \times 70 \times 70$ mesh). The iteration time $\Delta t$ is chosen as $0.005\tau$. Here the $\tau = \mu/p$ has the same order of magnitude as $\tau_{\text{FP}}$ and $\tau_{\text{ES}}$, but their values are not the same.
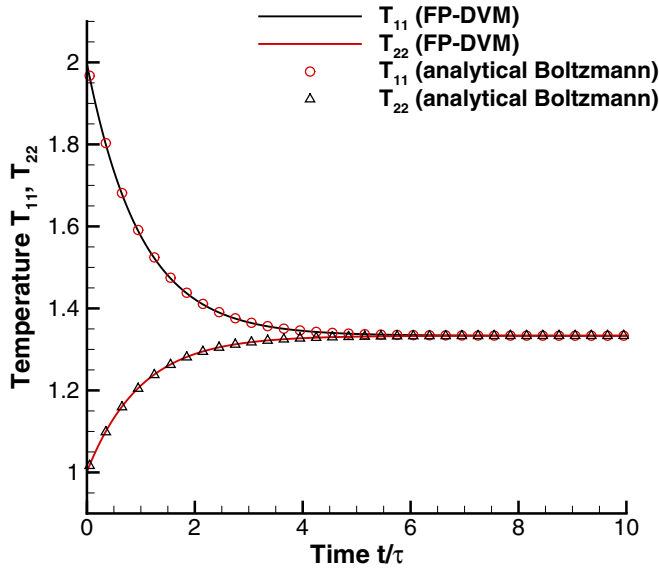
FIG. 3. The relaxation process of anisotropic temperatures with initial values $T_{11} = 2T_{22} = 2T_{33}$.

For the Maxwell molecule, the relaxation of stress and heat flux from the Boltzmann equation is [12]

$$\frac{\partial \tau_{ij}}{\partial t} = -\frac{\tau_{ij}}{\tau},$$
$$\frac{\partial q_i}{\partial t} = -\frac{\text{Pr}\, q_i}{\tau}. \tag{29}$$

For the homogenous case, since the density is a constant, the relaxation of anisotropic temperature can be derived from Eq. (29) as follows:

$$\frac{\partial T_{ij}}{\partial t} = -\frac{T_{ij} - T\,\delta_{ij}}{\tau}. \tag{30}$$

So the analytical solution of temperature and heat flux can be obtained as

$$T_{ij}(t) = e^{-t/\tau}\{T_{ij}(0) - T(0)\delta_{ij}\} + T(0)\delta_{ij},$$
$$q_i(t) = e^{-\text{Pr}\, t/\tau} q_i(0). \tag{31}$$

The relaxation process of distribution in the $3V$ space predicted by the present method is shown in Fig. 2, where the iso-surface of distribution gradually transforms from an ellipsoid to a sphere during several $\tau$. In Fig. 3, the relaxation process of anisotropic temperatures predicted by the present method matches precisely with the analytical solution [Eq. (31)].

### C. Relaxation of bi-model distribution function (0D-3V case)

In this case, the distribution function is composed of two Maxwellian distributions determined by the physical variables before and after the shock wave, respectively. According to the Rankine-Hugoniot relation for a Ma 8.0 shock wave, the physical variables before the shock are $u_{a,1} = 8.0$, $u_{a,2} = u_{a,3} = 0$, $T_a = 1.0$, and the physical variables after the shock wave are $u_{b,1} = 2.09$, $u_{b,2} = u_{b,3} = 0$, $T_b = 20.87$. The weights of two Maxwellian distributions are chosen as $\rho_a = 0.9$ and $\rho_b = 0.1$ to mimic the distribution function in the front of the shock wave, where high nonequilibrium

exists. This case investigates the relaxation of this highly nonequilibrium distribution function. The truncated discrete velocity space is $[-26, 26]$ in each direction with 260 discrete points ($260 \times 260 \times 260$ mesh). The iteration time $\Delta t$ is chosen as $0.001\tau$. The time evolution of this initial bi-model distribution is shown in Fig. 4, where two Maxwellian distributions merge into a single one during about $10\tau$. The evolutions of anisotropic temperatures and heat flux predicted by the present method are shown in Fig. 5, and they match with the analytical solution [Eq. (31)] precisely.

### D. Relaxation of discontinuous distribution function (0D-3V case)

The discontinuous distribution function in this case mimics the nonequilibrium distribution at the gas-solid boundary or in the Knudsen layer. It is composed of two half Maxwellian distributions. The interface of two half Maxwellian distributions in velocity space is the face $\xi_1 = 0$. Across the interface, the distribution is discontinuous. The Maxwellian distribution on the left is determined from $\rho_a = 1.0$, $u_{a,i} = 0$, $T_a = 2.0$, while the Maxwellian distribution on the right is determined from $\rho_b = 1.0$, $u_{b,i} = 0$, $T_b = 1.0$. This setting mimics the situation that the temperature of fluid is different from the temperature of the solid wall. The truncated discrete velocity space is $[-8, 8]$ in each direction with 80 discrete points ($80 \times 80 \times 80$ mesh). The iteration time $\Delta t$ is chosen as $0.005\tau$. The time evolution of the initial discontinuous distribution is shown in Fig. 6, where the discontinuity disappears during only one $\tau$, and gradually achieves equilibrium during several $\tau$. The evolutions of anisotropic temperatures and heat flux predicted by the present method are shown in Fig. 7. Due to the exponent term in Eq. (31), at first the distribution function approaches the equilibrium in a fast rate. This phenomenon can also be seen from the quick disappearance of discontinuity. Then the rate slows down when the distribution is near equilibrium.

### E. Normal shock wave structure (1D-quasi 1V case reduced from 1D-3V case)

Shock structure prediction is a benchmark test case for nonequilibrium flow models and corresponding numerical methods. In the macroscopic point of view, normal shock wave is a discontinuity in space, across which physical variables change suddenly. While, in the microscopic point of view (zoom into the thin shock wave), the physical variables in the shock wave changes smoothly from the front to the back of the shock wave. Physically, the molecules in the shock wave are composed of the molecules before the shock (super, hyper-sonic, low temperature) and the molecules after the shock (subsonic, high temperature). When shock Ma number is high, the separation of distribution functions before and after the shock in velocity space is large. Since the molecular collisions in the thin shock wave (about twenty m.f.p.) are insufficient, the distribution function will be far from equilibrium (high nonequilibrium).

The variable soft sphere (VSS) model is used in this case since it can be reduced to the hard sphere (HS) model and inverse power potential model directly by using their scattering factor $\alpha$ and heat index $\omega$. The m.f.p. of the VSS
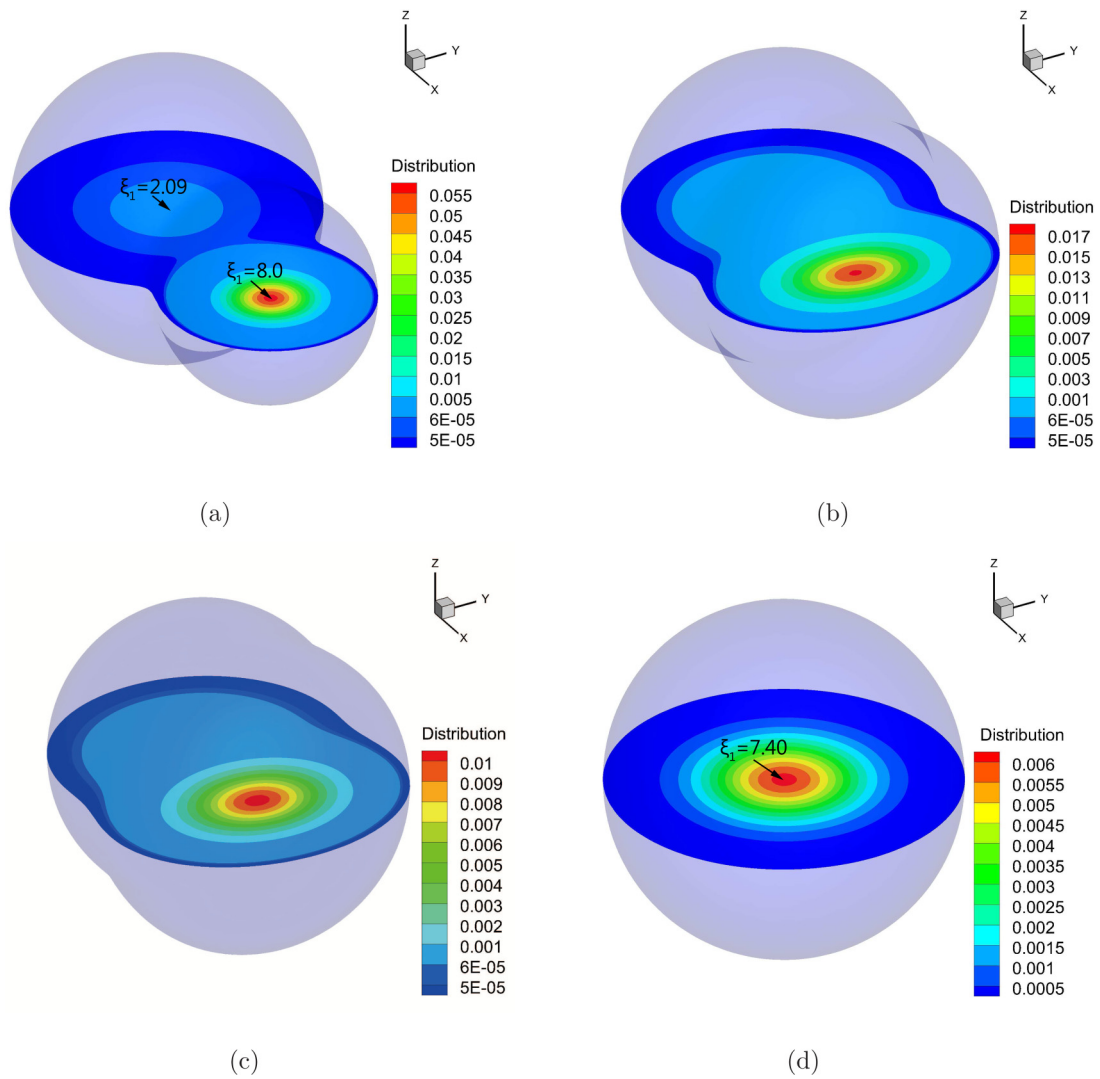
FIG. 4. The relaxation process of bi-model distribution, only the region with distribution function greater than (a)–(c) $5 \times 10^{-5}$ or (d) $5 \times 10^{-4}$ is plotted, and the contour is on the plane $\xi_3 = 0$. The evolution time $\tau$ is (a) 0, (b) 1, (c) 2, and (d) 10, respectively, in clockwise from the top-left figure.
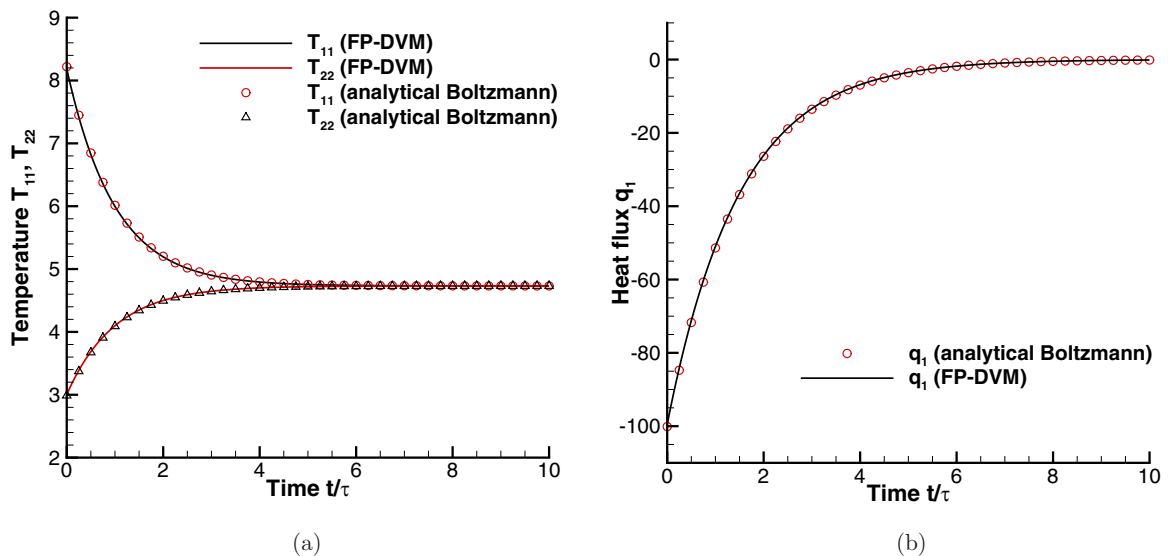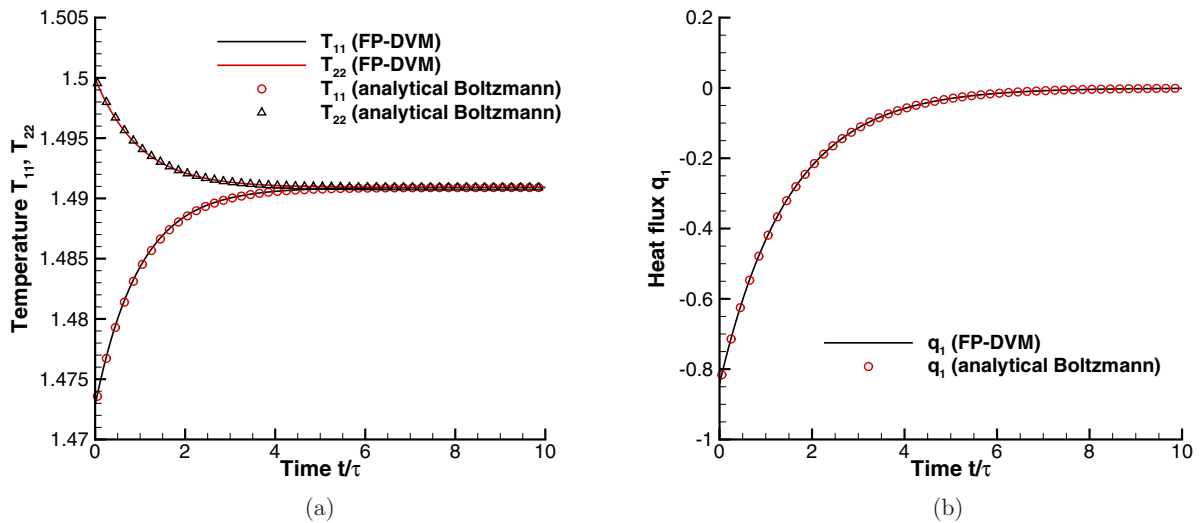


FIG. 5. The relaxation process of anisotropic temperatures and heat flux of initial bi-model distribution. The left figure is the (a) anisotropic temperatures, the right figure is the (b) heat flux.
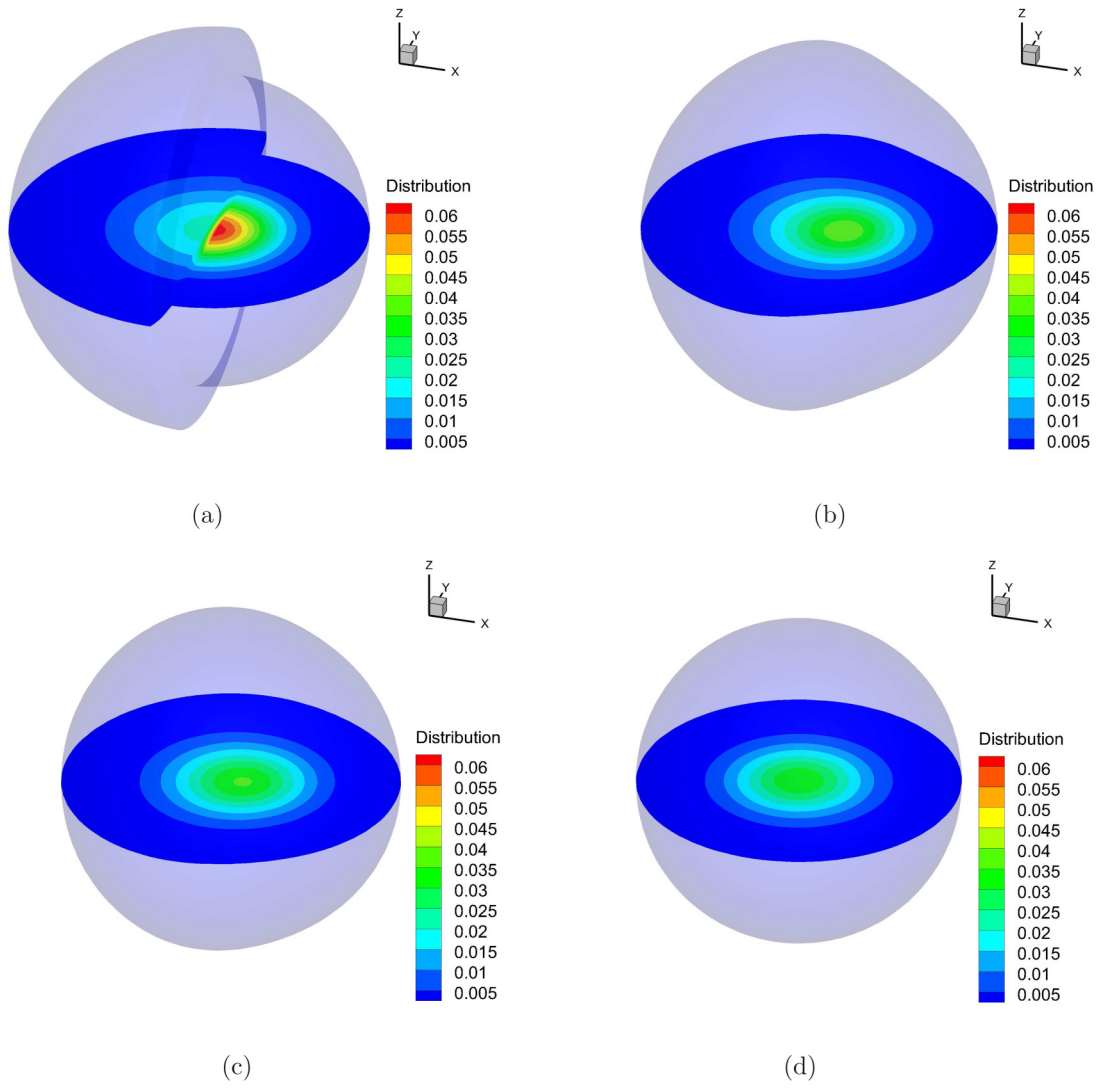
FIG. 6. The relaxation process of discontinuous distribution, only the region with distribution function greater than $5 \times 10^{-3}$ is plotted, and the contour is on the plane $\xi_3 = 0$. The evolution time $\tau$ is (a) 0, (b) 1, (c) 2, and (d) 10, respectively, in clockwise from the top-left figure.



FIG. 7. The relaxation process of anisotropic temperatures and heat flux of initial discontinuous distribution. The left figure is the (a) anisotropic temperatures, the right figure is the (b) heat flux.
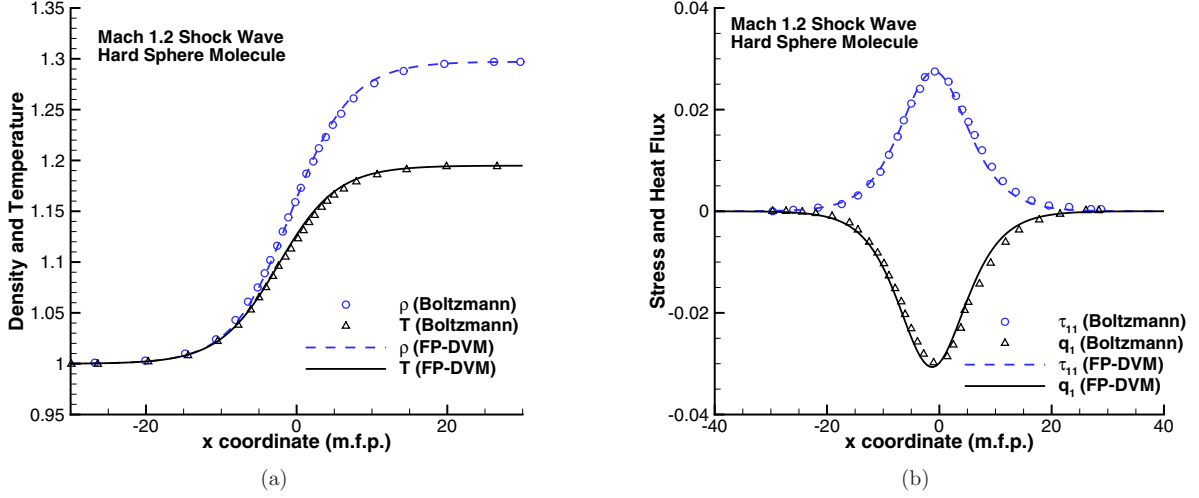
FIG. 8. The structures of density, temperature, stress, and heat in Ma $= 1.2$ shock wave. The left figure is the (a) density and temperature, the right figure is the (b) stress and heat flux.

model (denoted by $\lambda_m$) is defined as

$$\lambda_m = \frac{1}{\beta}\sqrt{\frac{RT}{2\pi}}\frac{\mu}{p}, \tag{32}$$

where $\beta$ is defined as

$$\beta = \frac{5(\alpha+1)(\alpha+2)}{4\alpha(5-2\omega)(7-2\omega)}. \tag{33}$$

In the shock structure case, the upstream and downstream conditions are determined by the Rankine-Hugoniot relation. The iteration time step of FP-DVM is chosen as

$$\Delta t = \min(\Delta t_{FP}, \Delta t_{TP}), \tag{34}$$

here the subscript "TP" stands for "transport" and corresponds to the free transport operator. $\Delta t_{FP}$ and $\Delta t_{TP}$ can be calculated using the following equation:

$$\Delta t_{FP} = a_{FP}\tau_{FP}\frac{\Delta\xi^2}{\max(RT)},$$
$$\Delta t_{TP} = a_{TP}\frac{\Delta x}{\max(\xi_i)}, \tag{35}$$

where $a_{TP}$ and $a_{FP}$ denote the Courant-Friedrichs-Lewy (CFL) numbers for the transport operator and collision operator, respectively.

### 1. Mach 1.2

In this case, the HS molecule model ($\omega = 0.5$, $\alpha = 1.0$) is used which is the same with the deterministic solution of the full-Boltzmann equation in Ref. [42]. For the full-Boltzmann solution, the $x$ coordinate is nondimensionalized using the m.f.p. of the HS molecule [42]. The density, temperature, stress, and heat flux in the shock wave are nondimensionalized using

$$\hat{\rho} = \frac{\rho}{\rho_{up}}, \quad \hat{T} = \frac{T}{T_{up}},$$
$$\hat{\tau}_{11} = -\frac{\tau_{11}}{p_{up}}, \quad \hat{q}_1 = \frac{q_1}{p_{up}\sqrt{2RT_{up}}}, \tag{36}$$

here subscripts "up" and "down" are used to indicate the variables in the upstream and downstream of the shock wave, respectively. The truncated discrete velocity space is $[-7\sqrt{RT_{up}}, 7\sqrt{RT_{up}}]$ with 70 points. The cell Knudsen number $Kn_{cell} = $ m.f.p.$/\Delta x$ is chosen as 4.0 (the cell length in physical space is a quarter of m.f.p.). $a_{FP}$ and $a_{TP}$ are set as 1.0 and 0.9, respectively. The density-temperature profile and stress-heat flux profile are illustrated in Figs. 8(a) and 8(b). The FP-DVM predictions match well with the full-Boltzmann result in Ref. [42]. In this case, the Ma number is low, and the nonequilibrium is not too strong.

### 2. Mach 3.0

The same HS model ($\omega = 0.5$, $\alpha = 1.0$) as the Ma 1.2 case is used here along with the same nondimensionalized $x$ coordinate and physical variable [Eq. (36)]. Comparing to the Ma 1.2 case, the degree of nonequilibrium increases in this case. The truncated discrete velocity is $[-10\sqrt{RT_{up}}, 10\sqrt{RT_{up}}]$ with 100 points. $Kn_{cell} = 4.0$ is used. $a_{FP}$ and $a_{TP}$ are set as 1.0 and 0.8, respectively. The density-temperature profile and stress-heat flux profile are illustrated in Figs. 9(a) and 9(b). The FP-DVM predictions match well with the full-Boltzmann result in Ref. [42], except that the temperature profile rises a little earlier, so are the stress and heat flux profiles.

### 3. Mach 8.0

The working gas is Argon in this case. When the Ma number is 8.0, the flow inside the shock wave is in high nonequilibrium. Being the same with Ref. [43], an eleventh power inverse power potential model is used, whose model coefficients can be calculated from Ref. [44] as $\omega = 0.68$, $\alpha = 1.4225$. The density, temperature, stress, and heat flux profiles are calculated and compared to the DSMC results in Ref. [43]. Instead of using the m.f.p. of the inverse power potential model and being the same with the setting in Ref. [43], the $x$ coordinates in the profiles are nondimensionalized using the m.f.p. of the HS molecule. The density and temperature are
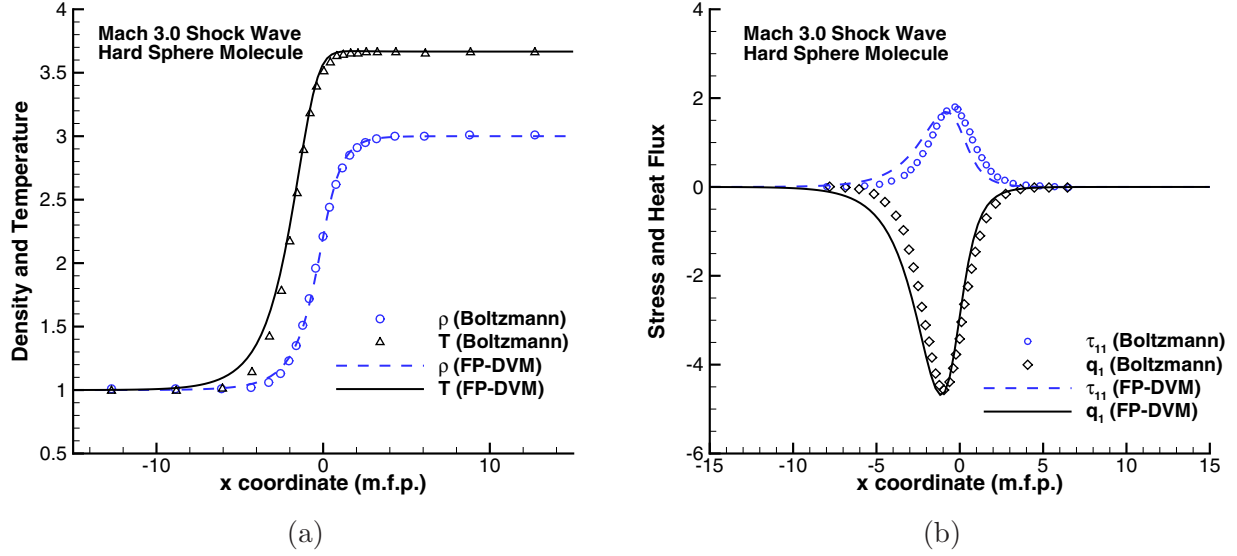
FIG. 9. The structures of density, temperature, stress, and heat flux in Ma = 3.0 shock wave. The left figure is the (a) density and temperature, the right figure is the (b) stress and heat flux.

normalized using

$$\hat{\rho} = \frac{\rho - \rho_{\text{up}}}{\rho_{\text{down}} - \rho_{\text{up}}}, \quad \hat{T} = \frac{T - T_{\text{up}}}{T_{\text{down}} - T_{\text{up}}}. \tag{37}$$

The stress and heat flux are nondimensionalized using

$$\hat{\tau}_{11} = -\frac{\tau_{11}}{\rho_{\text{up}}(2RT_{\text{up}})}, \quad \hat{q}_1 = \frac{q_1}{\rho_{\text{up}}(2RT_{\text{up}})^{3/2}}. \tag{38}$$

The truncated discrete velocity space is $[-30\sqrt{RT_{\text{up}}}, 30\sqrt{RT_{\text{up}}}]$ with 300 points, and the cell Knudsen number $\text{Kn}_{\text{cell}} = 4.0$. $a_{\text{FP}}$ and $a_{\text{TP}}$ are set as 1.0 and 0.6, respectively. The density-temperature profile and stress-heat flux profile are illustrated in Figs. 10(a) and 10(b) along with the numerical prediction using the BGK-type Shakhov model in Ref. [45]. The temperature, stress, and heat flux profiles predicted by the

Shakhov model deviate from the DSMC results in the front of the shock wave, while the FP-DVM predictions match well with the DSMC results in such a high Ma number and high nonequilibrium case.

Since the aim of the above cases is examining the validity of the present FP-DVM method, then the scope of the truncated velocity space and the amount of the discrete velocity points are set to be large. For the Ma 8.0 case, the velocity scope $[-25\sqrt{RT_{\text{up}}}, 25\sqrt{RT_{\text{up}}}]$ is sufficient. With different amounts of discrete velocity points in the $\xi_1$ direction (300, 200, 100, and 50 points, respectively), the numerical results predicted by FP-DVM are examined in Fig. 11. It can be seen that the results with different amount of discrete velocity points almost coincide with each other, except in the front of the shock wave where the results obtained using 50
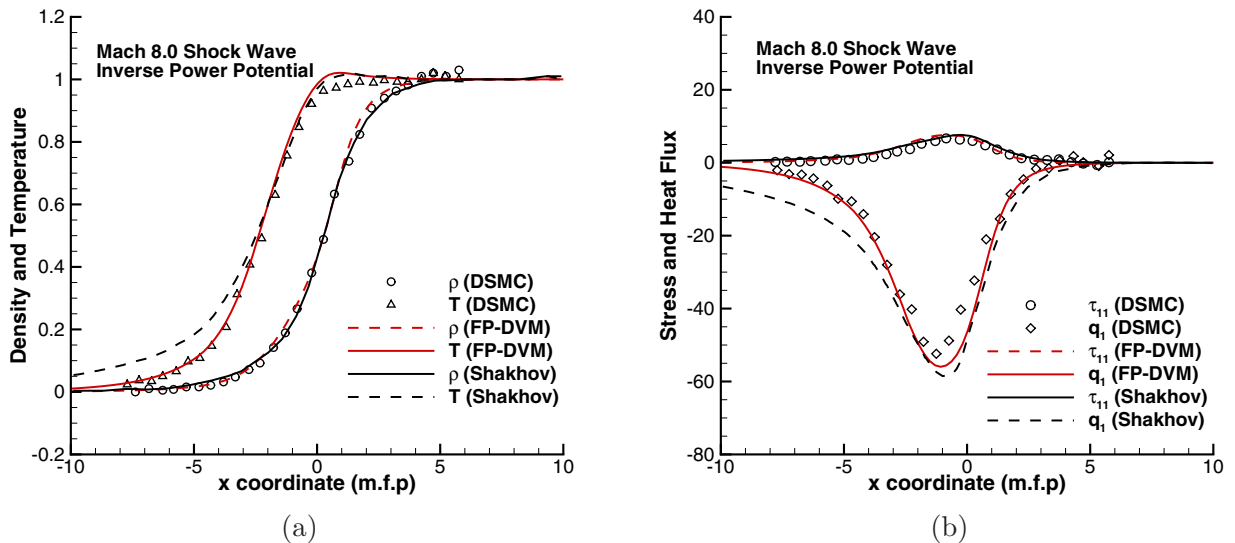


FIG. 10. The structures of density, temperature, stress, and heat flux in Ma = 8.0 Argon shock wave. The left figure is the (a) density and temperature, the right figure is the (b) stress and heat flux.
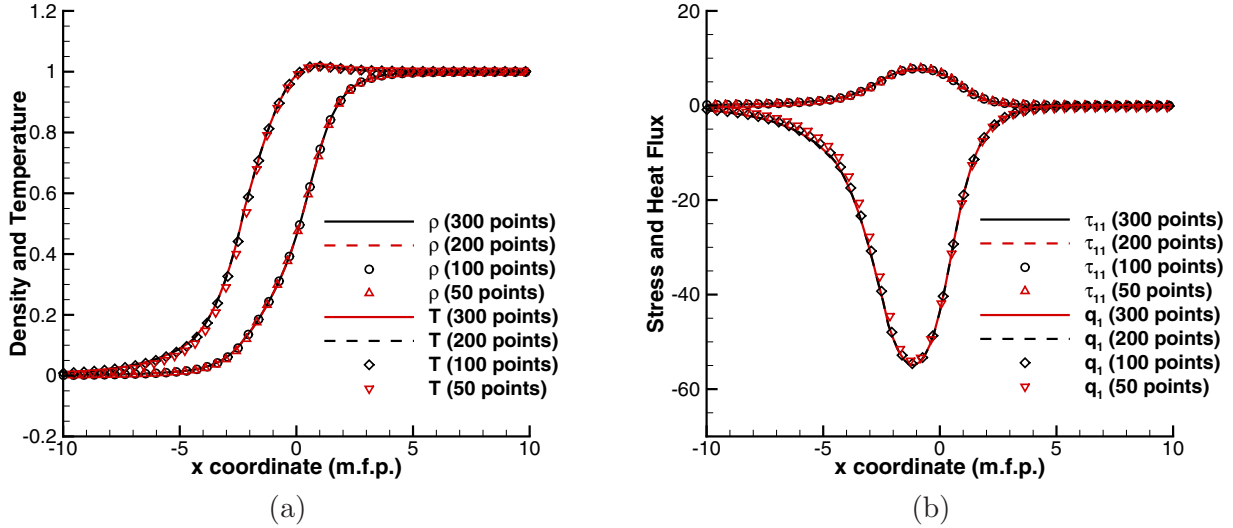
FIG. 11. The structures of density, temperature, stress, and heat flux in Ma = 8.0 Argon shock wave predicted by FP-DVM with different amount of discrete velocity points in $\xi_1$ direction. The left figure is the (a) density and temperature, the right figure is the (b) stress and heat flux.

discrete velocity points deviate sightly from the others. The distribution functions $F$ (mass distribution along $\xi_1$) and $G$ (energy distribution along $\xi_1$) at different locations inside the shock wave are shown in Fig. 12. They are predicted using 300 points and 50 points in the $\xi_1$ direction, respectively. Since this case is a high nonequilibrium one, the distribution functions inside the shock wave deviate much from the Maxwellian distribution. It can be seen from Fig. 12 that the positive property of distribution function is fulfilled in this high nonequilibrium case. It can also be seen in Fig. 12 that distributions predicted using 50 discrete velocity points match well with that predicted using 300 points. Since the discrete velocity space with 50 points is very coarse, its

resolution for precipitous distribution is low. For example, the setting of 50 discrete velocity points only has seven points for approximating the peak of $F$ at $x = -5$ [Fig. 12(a)], and may be the reason of slight deviations in the front of the shock wave (Fig. 11).

## V. CONCLUSION

In this paper, a deterministic FP-DVM method is proposed for the nonequilibrium flow simulations. The conservation problem of the discrete ES-FP equation is resolved by multiplying conservative coefficients whose differences with unity are small and have the same orders with the truncation error
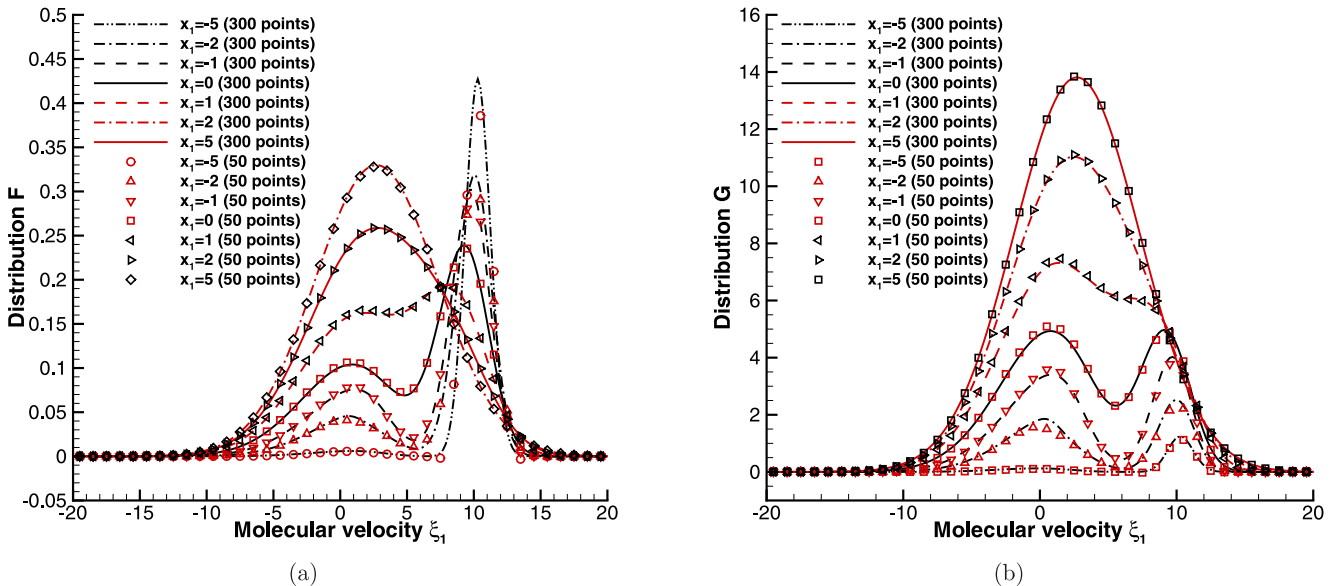


FIG. 12. The distribution function at different $x_1$ locations inside a Ma = 8.0 Argon shock wave predicted using 300 and 50 discrete velocity points in $\xi_1$ direction, respectively. The left figure is the (a) number distribution $F$, the right figure is the (b) energy distribution $G$.

of the difference scheme for ES-FP collision operator. Using four 0$D$-3$V$ cases which mimic different types of distributions that exist in real flow fields, the validity of the FP-DVM method and ES-FP model for homogenous cases are proved. In these cases, the evolution of nonequilibrium anisotropic temperatures and heat flux match with the analytical Boltzmann solution precisely. To further extend the scope to the ordinary inhomogeneous cases, a $nD$-quasi $nV$ reduction for the $nD$-3$V$ ($n < 3$) ES-FP equation is developed, which can greatly reduce the computational cost. Using the reduced 1$D$-quasi 1$V$ FP-DVM method, the shock structure cases from low to high Ma numbers are calculated. The negative distribution function and early rise of temperature profile for high Ma number cases do not appear in the present FP-DVM predictions. All the density, temperature, stress, and heat flux profiles match well with the direct full-Botlzmann results and DSMC results. The validity and accuracy of both FP-DVM and ES-FP model for nonequilibrium flow simulation are proved, and the shock structure profiles predicted by the FP-DVM method are probably the best numerical prediction using model Boltzmann equations up to now to the best of our knowledge. The advantages of the present FP-DVM method can be summarized as follows.

(1) The present method for the ES-FP equation does not suffer from the nonphysical negative distribution function.

(2) By using the ES-FP equation, the information of the derivatives in velocity space can be utilized, therefore, less discrete velocity points can be adopted.

(3) The ES-FP equation has a good model precision (such as in the high Ma number shock structure case).

Since the FP-type model equations have a stiffness problem, the penalty and implicit treatments used in previous research should be considered in the further works of the FP-DVM method to further increase its iteration time step. The time integral solution of BGK-type equations can also be used in the flux calculation of the present method to extend its scope to the whole flow regime (make it a UGKS-type method).

## ACKNOWLEDGMENTS

[1] S. Küchlin and P. Jenny, J. Comput. Phys. **328**, 258 (2017).

[2] M. H. Gorji and P. Jenny, J. Comput. Phys. **287**, 110 (2015).

[3] J. Mathiaud and L. Mieussens, J. Stat. Phys. **162**, 397 (2016).

[4] M. N. Rosenbluth, W. M. MacDonald, and D. L. Judd, Phys. Rev. **107**, 1 (1957).

[5] L. D. Landau, The kinetic equation in the case of coulomb interaction, Technical Report No. AD0667650, General Dynamics/Astronautics, San Diego, CA, 1958.

[6] P. Degond and B. Lucquin-Desreux, Numer. Math. **68**, 239 (1994).

[7] A. Kompaneets, Sov. Phys. JETP **4**, 730 (1957).

[8] Y. B. Zel'dovich, E. Levich, and R. Syunyaev, Sov. Phys. JETP **35**, 733 (1972).

[9] L. Zeng and T. Pedley, J. Fluid Mech. **852**, 358 (2018).

[10] M. Dolfin, L. Leonida, and N. Outada, Phys. Life Rev. **22**, 1 (2017).

[11] G. Toscani, A. Tosin, and M. Zanella, Phys. Rev. E **98**, 022315 (2018).

[12] C. Cercignani, Appl. Math. Model. **14**, 613 (1990).

[13] G. A. Bird, *The DSMC Method* (CreateSpace Independent Publishing Platform, 2013).

[14] J. S. Chang and G. Cooper, J. Comput. Phys. **6**, 1 (1970).

[15] C. Buet and K. C. L. Thanh, hal-00142408v3 (2007).

[16] E. S. Yoon and C. S. Chang, Phys. Plasmas **21**, 032503 (2014).

[17] E. W. Larsen, C. D. Levermore, G. C. Pomraning, and J. G. Sanderson, J. Comput. Phys. **61**, 359 (1985).

[18] E. M. Epperlein, J. Comput. Phys. **112**, 291 (1994).

[19] W. T. Taitano, L. Chacón, A. N. Simakov, and K. Molvig, J. Comput. Phys. **297**, 357 (2015).

[20] W. T. Taitano, L. Chacón, and A. N. Simakov, J. Comput. Phys. **339**, 453 (2017).

[21] N. Crouseilles and F. Filbet, J. Comput. Phys. **201**, 546 (2004).

[22] F. Filbet and L. Pareschi, J. Comput. Phys. **179**, 1 (2002).

[23] R. Duclous, B. Dubroca, F. Filbet, and V. Tikhonchuk, J. Comput. Phys. **228**, 5072 (2009).

[24] K. Xu and J. Huang, J. Comput. Phys. **229**, 7747 (2010).

[25] Z. Guo, K. Xu, and R. Wang, Phys. Rev. E **88**, 033305 (2013).

[26] A. Peng, Z. Li, J. Wu, and X. Jiang, J. Comput. Phys. **327**, 919 (2016).

[27] L. M. Yang, Z. Chen, C. Shu, W. M. Yang, J. Wu, and L. Q. Zhang, Phys. Rev. E **98**, 063313 (2018).

[28] L. Yang, C. Shu, W. Yang, Z. Chen, and H. Dong, Phys. Fluids **30**, 062005 (2018).

[29] C. Liu and K. Xu, Commun. Comput. Phys. **22**, 1175 (2017).

[30] Z. Guo and K. Xu, Int. J. Heat Mass Transf. **102**, 944 (2016).

[31] S. Liu and C. Zhong, Phys. Rev. E **89**, 033306 (2014).

[32] V. A. Titarev, M. Dumbser, and S. Utyuzhnikov, J. Comput. Phys. **256**, 17 (2014).

[33] L. Yang, C. Shu, W. Yang, J. Wu, and M. Q. Zhang, Int. J. Numer. Methods Fluids **90**, 545 (2019).

[34] D. Jiang, M. Mao, J. Li, and X. Deng, Adv. Aerodyn. **1**, 8 (2019).

[35] R. Yuan and C. Zhong, arXiv:1810.13039 (2018).

[36] G. M. Kremer, *An Introduction to the Boltzmann Equation and Transport Processes in Gases* (Springer, Berlin, 2010), pp. 105–120.

[37] C. Buet and S. Cordier, J. Comput. Phys. **179**, 43 (2002).

[38] C. K. Chu, Phys. Fluids **8**, 12 (1965).

[39] J. Yang and J. Huang, J. Comput. Phys. **120**, 323 (1995).

[40] L. M. Yang, C. Shu, J. Wu, and Y. Wang, J. Comput. Phys. **306**, 291 (2016).

[41] L. M. Yang, C. Shu, J. Wu, and Y. Wang, Comput. Fluids **146**, 125 (2017).

[42] T. Ohwada, Phys. Fluids A **5**, 217 (1993).

[43] G. A. Bird, Phys. Fluids **13**, 1172 (1970).

[44] K. Koura and H. Matsumoto, Phys. Fluids A **3**, 2459 (1998).

[45] K. Xu and J.-C. Huang, IMA J. Appl. Math. **76**, 698 (2011).